Film-Drainage, Separation and Dissolution of Al_2O_3 Inclusions Across Interfaces between Molten Steel and Ladle-, Tundish- and Mold–Slags

G.N. Shannon and Seetharaman Sridhar

Carnegie Mellon University
Department of Materials Science and Engineering
Pittsburgh, PA 15213
USA

(Received August 27, 2004)

ABSTRACT

This paper presents calculations on the separation times for solid spherical, octahedral and plate-like micro-inclusions across interfaces between molten low carbon steel and ladle-, tundish-, and mold-slags. The effect of inclusion shape on the interfacial capillary force that arises due to the dynamic interfacial energy change during separation has been investigated and it is shown that this has a significant effect on whether the inclusion separates rapidly or settles at the interface. In the case of settled particles, the inclusion dissolution time was computed based on experimental data. For the slags considered, the most significant physical property was found to be the slag viscosity, which resulted in fast separation for the mold and ladle slag when compared to the more viscous tundish slag.

INTRODUCTION

Non-metallic inclusions in metallic melts are often removed by absorption into a slag phase. This slag phase is usually a molten mixture of SiO_2, Al_2O_3, and metal oxides. In the case of steel manufacturing, this is done in the ladle furnace, tundish, or continuous casting mold and involves three steps; (i) flotation of the inclusion to the steel melt/slag interface, (ii) separation into the slag phase and in some cases (iii) dissolution in the slag phase. Among the three steps for inclusion removal, the second step – separation across the interface – is the least understood and is strongly influenced by both interfacial and bulk fluid properties. The thermodynamics of inclusion removal have been described in a number of papers /1,2,3,4,5/. Consider an inclusion at the slag/metal interface. For the inclusion to be removed it is necessary for it to travel through the slag/metal interface, and on into the bulk slag phase. A favorable separation will be achieved, from a thermodynamic viewpoint, when the sum of changes in the various terms related to interfacial energies (γ) is negative and describes a favorable process, i.e.:

(i) For a thin solid inclusion to emerge at the slag/steel melt interface:

$$\Delta G = \gamma_{SI} - \gamma_{MS} - \gamma_{MI} < 0 \qquad (1)$$

where the subscripts *S*, *I*, and *M* denote slag, inclusion, and liquid metal phases respectively. Only the two flat surfaces of the inclusion are considered.

(ii) For the total emergence of this inclusion into the slag:

$$\Delta G = \gamma_{SI} + \gamma_{MS} - \gamma_{MI} < 0 \qquad (2)$$

While this model for separation of inclusions across a metal/slag interface is based on thermodynamics, it is rather simplified and thus its applicability is limited. This is primarily due to two significant issues. Firstly, inclusions are, in general, not thin. Thus during the separation, the interfacial energy of the system will

change continuously (and abruptly) according to:

$$G = A_{SI} * \gamma_{SI} - A_{MS} * \gamma_{MS} - A_{MI} * \gamma_{MI} \quad (3)$$

due to the three area terms. Thus, depending on the inclusion geometry, the change in free energy in terms of the degree of separation will have a distinct behavior and, as a result, so will the interfacial capillary force:

$$F_{\sigma,z} = -\frac{dG}{dZ} \quad (4)$$

Secondly, at distances close to the interface, the assumption of a continuous medium is no longer valid /6,7/ and the thin liquid film ahead of the particle will be removed more slowly. The residence time of particles at a fluid/fluid interface may thus be long even though it is energetically favorable to separate it from one phase to the other.

In the case of solid inclusions, the film drainage is primarily a hydrodynamic problem, while the subsequent separation depends largely on the interfacial capillary force (Equation (4)). Bouris and Bergeles /8/ and Nakajima and Okamura /9/ have models predicting the separation times for spherical, rigid, chemically inert particles.

In this paper, the effects of particle dissolution and shape are introduced into the models of Bouris and Bergeles /8/ and Nakajima and Okamura /9/. The kinetics of dissolution play a role when the interfacial tensions do not allow for complete separation. The shapes considered, besides spheres, are octahedrons and plates.

SOURCES, SHAPES, AND SIZES OF Al_2O_3 INCLUSIONS IN STEELS

Alumina (Al_2O_3) inclusions are the result of either intentional de-oxidation reactions between oxygen and aluminum alloying additions in the ladle, or subsequent unwanted interactions between un-reacted but dissolved aluminum and its environment (such as refractory, gas atmosphere, or slag). The former are denoted endogenous inclusions whereas the latter are exogenous inclusions.

Depending on the precipitation conditions and subsequent evolution (crystal growth or agglomeration) the resulting inclusions can exhibit a variety of morphologies. Spheres, polyhedra, plates, dendrites, and clusters have been reported. According to a recent study /10/ where inclusions in different carbon steel grades as sampled from the ladle were characterized, high super-saturation leads to the formation of spherical particles, or – when impurity absorption took place – plate-like particles. Non-uniform super-saturation over the particle surface leads to dendrite formation. Under low super-saturation, near equilibrium conditions, the particles were found to become facetted. When simultaneous growth and sintering occurred, the particles assumed octahedral forms. The average sizes of the different inclusions showed that spherical inclusions were 0.5 and 2.6 μm in diameter, octahedral inclusions were 2.4 μm, non-octahedral polyhedra were 2.4 μm or larger than 5 μm, plates were of 2.9 μm length and less than 0.1 μm thickness, dendrites were 5-20 μm across and clusters and agglomerates varied in size.

THEORETICAL BACKGROUND

The original model developed by Nakajima and Okamura assumed that (i) the separating solid spherical inclusion maintained its size and shape (radius=R_I), (ii) both steel and slag are incompressible, isothermal fluids, (iii) a steel film is formed ahead of the inclusion when the impact Reynolds number $Re > 1$; this film would have a concentric shape with negligible flow in the radial direction, (iv) the film would drain according to a stream function (ψ) expression along the sphere in spherical coordinates:

$$\psi = -\frac{1}{2}\frac{dZ}{dt}\left(-\frac{3}{2}rR_I + \frac{1}{2}\frac{R_I^2}{r}\right)\sin^2\theta \quad (5)$$

Furthermore, (v) the effect of interface deformation on the interfacial tension is neglected. (vi) The film would rupture when a thickness of 0.001*inclusion radius (R_I) is reached. Finally, (vii) the following forces acting on the inclusion are considered (Figure 1 and

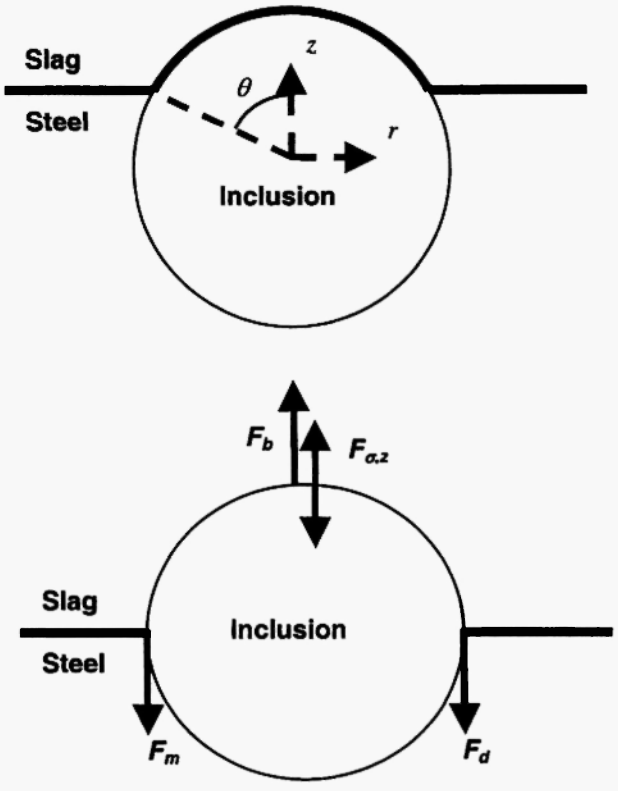

Fig. 1: Forces acting on a particle

Equations (4) and (6-8)):

F_b is the buoyant force, given by:

$$F_b = V_I g \cdot f\left(Z, \rho_m, \rho_s\right) \tag{6}$$

where the function f takes into account the contributions from the slag and molten metal phases and depends upon inclusion volume and the degree of separation (Z).

F_d is the drag force, given for unspecified inclusion geometry by:

$$F_d = C_d A_I \frac{1}{2} \rho_M \left(\frac{dZ}{dt}\right)^2 \cdot h(Z, \eta_S, \eta_M) \tag{7}$$

Here, C_d is the friction factor in the metal or slag. The function h takes into account the interfacial areas of each phase touching the inclusion to properly calculate the contributions from each molten phase to the drag force. It should be noted that Equation (7) assumes that the dependence of C_d on Re is the same in both molten phases. If it is not, then, Equation (7) will have to be split into two factors, where each contains a function of the type h. η_M and η_S are the static viscosities of metal melt and slag respectively.

The damping of the acceleration due to the fluid ahead of the inclusion is given by:

$$F_m = C_m V_I f\left(Z, \rho_M, \rho_S\right) \frac{d^2 Z}{dt^2} \tag{8}$$

where C_m is close to 0.5 and f has the same significance as for Equation (6).

The interfacial capillary force, $F_{\sigma,z}$, is given by Equation (4), in its most general form.

The inclusion acceleration is given by the force balance through Newton's second law:

$$V_I \rho_I \frac{d^2 Z}{dt^2} = \sum_i F_i \tag{9}$$

To obtain the inclusion position with time, the differential equation (Equation (9)) has to be solved. During the period that a steel film exists, forces given by Equations (6) through (8) are constant (at least with respect to position) and dependent on the metal only, whereas the interfacial capillary force (Equation (4)) will change as the interface meniscus is deformed. The solution must in this case also satisfy the stream line function, Equation (5). When a steel film is not formed or after the film has ruptured, Equation (5) is not relevant but now Equations (4) and (6) through (8) all depend on Z, since the inclusion is in partial contact with both steel melt and slag, and the ratio between the inclusion areas and volumes that are within each of the two molten phases changes during separation.

EFFECTS OF MENISCUS

The previous investigators have assumed that beyond the concentric shell of a draining steel film, there is no interface deformation. Since the interfacial forces are expected to play a considerable role, it is doubtful whether this assumption is true. Depending on the interfacial tension force balance at the

steel/slag/inclusion interface, a meniscus will form and the interface would be described by Figure 2, rather than by Figure 1.

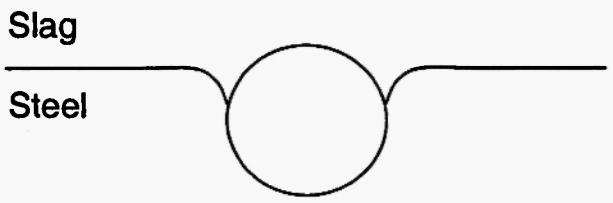

Fig. 2: Meniscus formation

This will have the following consequences. Firstly, the slag/molten steel interface changes as the triple phase contact point shifts position during separation, affecting Equations (3) and (4). Secondly, inclusion shapes with sharp edges would necessitate discontinuous steps in the meniscus shape over time and thus also for Equation (3) and (4). This complication is described in Figure 3 for an octahedron. The edge could, in these cases, drag the meniscus along rather than release it and allow it to establish a new contact angle at the other side of the edge – this would occur as shown as profile B in Figure 3.

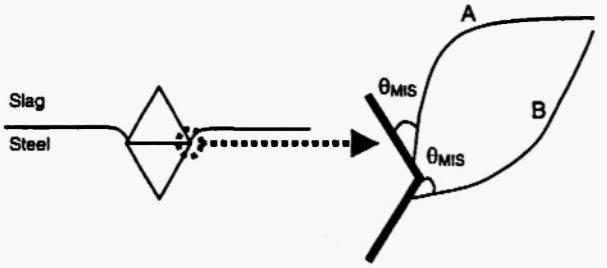

Fig. 3: Meniscus formation and discontinuous change at a sharp edge of an octahedral inclusion

While it is expected to be important, the meniscus and associated edge effects are not considered in this paper since it is difficult to estimate the metal/inclusion/slag contact angle.

PERTINENT PHYSICAL PROPERTIES

Relevant properties of a low carbon, aluminum killed steel were chosen for the molten steel phase. Three synthetic slag compositions were chosen to represent ladle-, tundish-, and mold-slags. Systems where Al_2O_3 inclusion dissolution rates were experimentally determined in earlier studies /11,12/ dictated these choices. L-Slag consists of 36 wt% Al_2O_3, 59 wt% CaO and 5 wt% SiO_2 and represents a ladle slag. T-Slag consists of 21 wt% Al_2O_3, 36 wt% CaO, 42 wt% SiO_2 and 0.4 wt% MgO and was chosen to represent a tundish slag. In the case of the mold slag composition, a fluorine-less slag of composition 20 wt% CaO, 10 wt% Al_2O_3, 40 wt% SiO_2 , 10 wt% MgO, 20 wt% Na_2O, 1 wt% Li_2O, and 1.5 wt% B_2O_3 was chosen. It should be noted that this slag represents an experimental composition rather than those used commonly in continuous casting molds; this slag was chosen since dissolution rates as well as physical properties are difficult to determine when fluorine is added, due to evaporation losses.

Physical bulk and interfacial properties for the slags were evaluated from the Slag Atlas /13/, except for the viscosity of the fluorine less mould slag which was experimentally determined in an earlier study /11/. Molten steel properties were obtained from ref. /14/. The properties are listed in Tables I and II. Note that the interfacial tension between inclusion and slag is

Table I
Properties of the molten phases

Fluid	Density (kg/m^3)	Viscosity (Pa s)	Interfacial Tension (N/m)
Steel	7000	0.006	NA
L-Slag	2700	0.0562	$\sigma_{MS} = 1.2$
T-Slag	2560	0.600	$\sigma_{MS} = 1.16$
M-Slag	2750	0.0631	$\sigma_{MS} = 1.12$

Table II
Al_2O_3 inclusion and inclusion/fluid properties

Density (kg/m^3)	Inclusion Interfacial Tension (N/m) with:			
	Steel	L-Slag	T-Slag	M-Slag
3990	$\sigma_{MI} =$ 1.57	$\sigma_{SI} =$ 0.01	$\sigma_{SI} =$ 0.01	$\sigma_{SI} =$ 0.01

considered too difficult to determine experimentally, and is chosen to be near zero because of their structural similarity. Later, this value is modified to examine system dependencies.

The calculations assumed that all inclusion shapes had an equivalent volume that corresponded to that of a sphere with a diameter of 3 μm (later, a spherical inclusion with a diameter of 10 microns is used). The thickness of the square plate was assumed to be 1/30 of the length. Thus the octahedron will have an edge length of 3.11 μm, and the plate will have dimensions of 7.5 μm by 7.5 μm by 0.25 μm. In terms of orientation, it is assumed the octahedron is rising point-first, while the plate can rise in two cases; vertically, and horizontally.

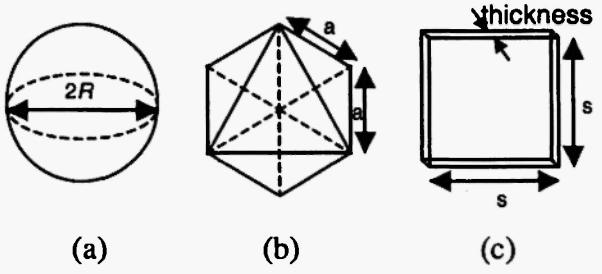

Fig. 4: Inclusion shapes considered: (a) Sphere, (b) Octahedron, and (c) Plate

Transport properties are affected by inclusion shape, relative speeds and viscosities, and by coefficients of drag and of added mass. For a sphere in liquid metal, the impact Reynolds number is given by:

$$\mathrm{Re} = U \cdot 2R_I \cdot \rho_M / \mu_M \tag{10}$$

where U is the impact velocity, and ρ_m and μ_m are the metal density and viscosity, respectively. For different shapes, the radius of a sphere with an equivalent volume is chosen.

The impact velocity, U, can often be taken to be the terminal rise velocity for a sphere in the melt, given by:

$$U_{term} = (2/9) \cdot R_I^2 \cdot (\rho_M - \rho_I) \cdot g / \mu_M \tag{11}$$

where g is acceleration due to gravity and ρ_I is the density of the inclusion. Again, the radius of a 3 micron sphere of equivalent volume is assumed for other shapes. Because of these assumptions, equivalent volumes will have the same initial impact Reynolds number, since only one inclusion and metal composition is assumed. Because of our choice of inclusion size here, the Reynolds number is low enough not to create a steel film.

The coefficient of drag, C_d, is taken as $24/Re$ for the cases of the sphere and octahedron, which includes both friction and form drag for laminar flow. However, for a rising, vertical plate, only friction drag need be considered, as the plate is assumed to have negligible thickness relative to its other dimensions. Thus, for a vertical plate, $C_d = 16/Re$.

The coefficient of added mass, C_m, is taken to be 0.5, a typical value for a moving sphere. The rising vertical plate is considered to have negligible fluid mass force, due to its thin profile.

METHOD OF COMPUTATION

Because of its dynamic state, and dependence on inclusion shape, the capillary force is examined in more detail. Interfacial energies are given in Equations (12) through (15) for the various inclusion geometries. Note that because of its discontinuity, the octahedron has two descriptions of its position.

For the sphere:

$$E_{\sigma,Z} = [\pi R_I^2 - \pi(2R_I Z - Z^2)]\sigma_{MS} + [2\pi R_I Z]\sigma_{SI} + [4\pi R_I^2 - 2\pi R_I Z]\sigma_{MI} \tag{12}$$

For the two cases for the octahedron:

for $Z < a\sqrt{2}$:

$$E_{\sigma,Z} = (a^2 - 2Z^2)\sigma_{MS} + (2Z^2\sqrt{3})\sigma_{IS} + (2a^2\sqrt{3} - 2Z^2\sqrt{3})\sigma_{MI} \tag{13}$$

for $Z > a\sqrt{2}$:

$$E_{\sigma,Z} = [a^2 - (4a^2 - 4\sqrt{2}aZ + 2Z^2)]\sigma_{MS} + 2\sqrt{3}(2a^2 - 2\sqrt{2}aZ + Z^2)\sigma_{MI} + [2a^2\sqrt{3} - 2\sqrt{3}(2a^2 - 2\sqrt{2}aZ + Z^2)]\sigma_{SI} \tag{14}$$

For the vertical plate:

$$E_{\sigma,Z} = 2s(s - Z)\sigma_{IM} + 2sZ\sigma_{IS} \tag{15}$$

In the case of the horizontal plate, because a negligible thickness is assumed, there is only one separation state to consider. Thus, its interfacial energy is constant and irrespective of Z.

Figures 5, 7, and 9 plot the energy as a function of separation distance for each of the shapes and orientations mentioned above, for L-, T-, and M-slags, respectively.

Expressions for the interfacial capillary force for various inclusion geometries are given in Equations (16)-(19), as derived from Equation (4).

For the sphere:

$$F_{\sigma,Z} = (-2\pi R_I + 2\pi Z)\sigma_{MS} + 2\pi R_I \sigma_{SI} - 2\pi R_I \sigma_{MI} \quad (16)$$

For the octahedron:

for $Z < a\sqrt{2}$:

$$F_{\sigma,Z} = -4Z\sigma_{MS} + 4\sqrt{3}Z\sigma_{IS} - 4\sqrt{3}Z\sigma_{MI} \quad (17)$$

for $Z > a\sqrt{2}$:

$$F_{\sigma,Z} = (4\sqrt{2}a - 4Z)\sigma_{MS} - 4\sqrt{6}a - 4\sqrt{3}Z)\sigma_{MI} + (4\sqrt{6}a - 4\sqrt{3}Z)\sigma_{SI} \quad (18)$$

For the vertical plate:

$$F_{\sigma,Z} = -2s\sigma_{IM} - 2s\sigma_{SI} \quad (19)$$

And for the horizontal plate, because the interfacial energy is not dependent on Z, the capillary force will be zero.

Figures 6, 8, and 10 show the capillary force as a function of separation distance for each of the shapes and orientations described, for L-, T-, and M-slags, respectively.

To solve the inclusion displacement requires solution of Equation (9), given proper force equations for the different inclusions shapes and conditions. The final equation is solved for particle acceleration as a function of speed and penetration.

Because the initial state of the particle is known (Z begins at 0, and the initial speed is given by U_{term} or a user-selected velocity), the acceleration solution can be solved numerically by using a small enough time step to increment both position and speed. In this manner, the particle's separation across the interface, as a function of time, can be known.

INCLUSION DISSOLUTION KINETICS

Because oxide inclusions and primarily oxide slag materials come in contact with each other, dissolution of the inclusion into the slag can occur, through kinetics described elsewhere /11,12/. This mechanism assumes a classical shrinking core model in which two rate-limiting reactions are considered, a surface reaction, and boundary layer diffusion in the Stokes regime. Different slags were found to be controlled by different contributions of each, thus, normalized inclusion radius is given by:

$$\frac{R_I}{R_o} = 1 - \left(\frac{t}{\tau}\right)^b \quad (20)$$

where R_o is the original inclusion radius, R_I is the current inclusion radius, t is time, τ is the necessary dissolution time (slag and temperature dependent) and b is the rate-limiting reaction factor, varying between 1 for a surface reaction and 0.5 for boundary layer diffusion. Both τ and b are experimentally determined. Table III lists the free particle dissolution times as well as reaction factor b for each of the slags, for a 3 μm diameter inclusion.

Table III
Dissolution kinetics properties for a 1.5 micron free-floating inclusion of 1.5 μm radius

	τ (milliseconds)	b
L-Slag	0.371	0.8
T-Slag	0.499	0.6
M-Slag	0.0827	1

If the particle reaches a stable point in its separation across the interface, this dissolution will still occur, but its reaction area will only include the portion of the inclusion in contact with the slag. Therefore its required dissolution time will be larger by the same factor that the exposed area is reduced. In this case, it is assumed that b will remain the same.

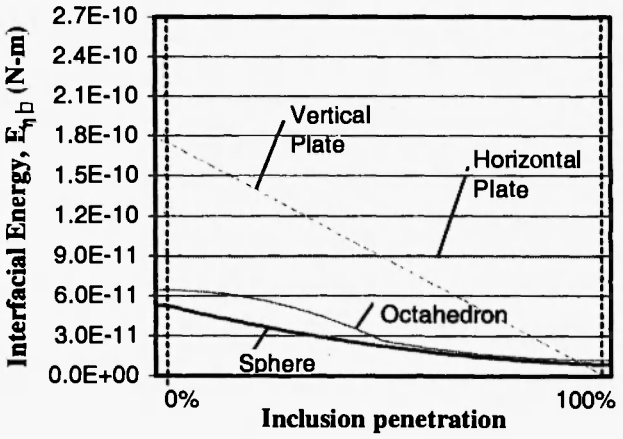

Fig. 5: Interfacial energy during separation for various inclusion geometries for L-Slag

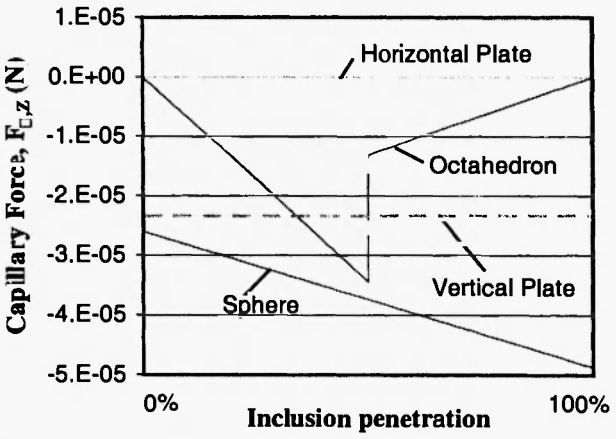

Fig. 6: Capillary force during separation for various inclusion geometries for L-Slag

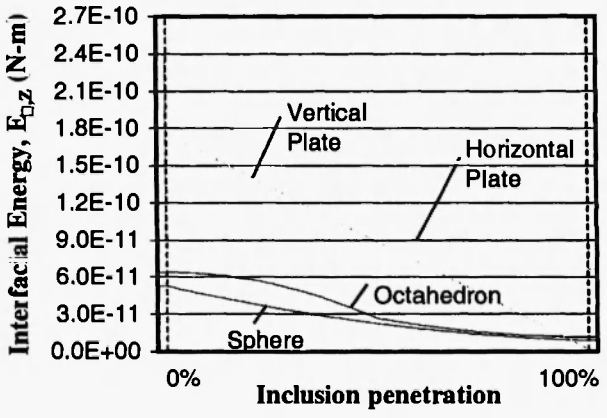

Fig. 7: Interfacial energy during separation for various inclusion geometries for T-Slag

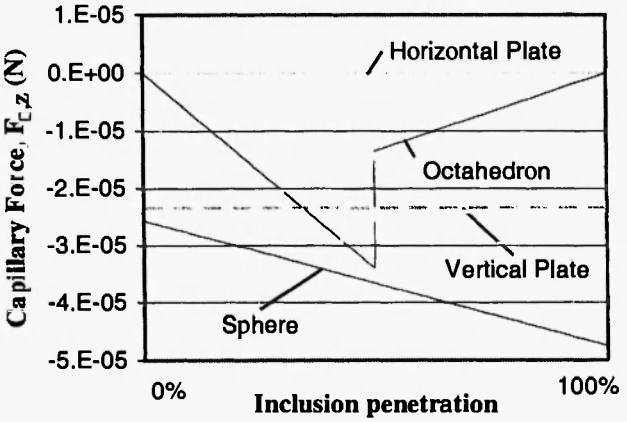

Fig. 8: Capillary force during separation for various inclusion geometries for T-Slag

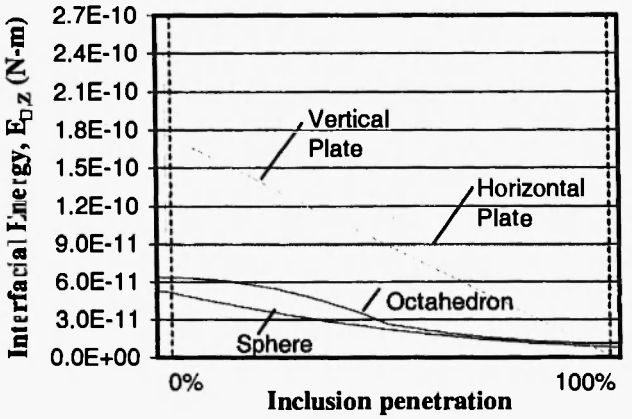

Fig. 9: Interfacial energy during separation for various inclusion geometries for M-Slag

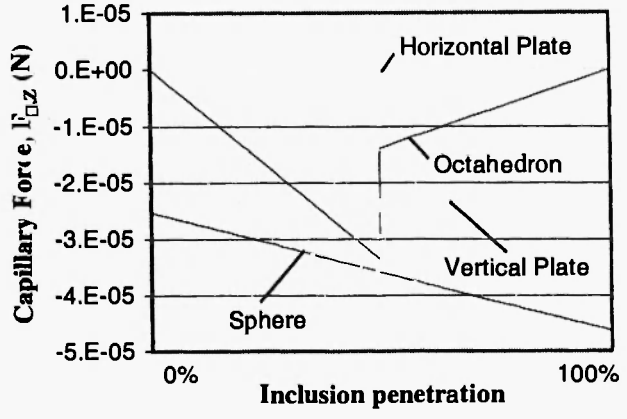

Fig. 10: Capillary force during separation for various inclusion geometries for M-Slag

RESULTS AND DISCUSSIONS

Because the specific value of σ_{IS} – the slag/inclusion interfacial energy – is difficult to measure experimentally, two different values are used for comparison purposes during separation modeling. The original value, 0.01 N/m, is treated as a minimal value. A second value, that of 0.6 N/m, has been introduced to induce the inclusion to settle at the interface. This is likely due to the creation of a minimum point on the interfacial energy curve for the spherical inclusion.

Figures 11 and 12 show separation curves for each of the σ_{IS} values for the octahedron, similarly Figures 13 and 14 for the vertical plate, and Figures 15 and 16 for the sphere – these latter two charts include dissolution results. The horizontal plate, because we have assumed a negligible thickness, only has one state of separation, and was considered too trivial a case to compare.

It is interesting to note that in the case of the octahedron (Figure 11 and 12), the inclusion moves fairly slowly at first and again once it nears penetration completion – this would seem to behave similarly to the octahedron's capillary force plot, which shows the force going to zero at either end of the separation range. Thus, an appreciable capillary force would seem to be necessary (perhaps even sufficient) for separation, at least in the case of the octahedron. While the plots seem to suggest that the octahedron appears to settle at a penetration level, this level is in fact beyond complete separation of the particle.

It is also apparent that while the sphere and octahedron have somewhat similar separation times, their manner of separation is much different – whereas the sphere separates relatively smoothly, the octahedron is slow to start, slow to end, and quite quick in the mid-separation range.

The vertical plate (Figure 13 and 14) passes into the slag quite easily, likely due to the lack of damping forces acting on it.

Unlike the other particles, the sphere was found to settle at a point of incomplete separation for the larger σ_{IS} value. The degree of separation once settling had occurred was found to be: for the L-Slag, 90.3%; for the T-Slag, 91.7%; and for the M-Slag, 93.3%. Practically, the particle will not remain trapped at the interface forever, even dismissing shear forces, due to dissolution. Therefore, Figures 15 and 16 (plotted on a log time scale) also includes dissolution curves for the settled sphere. Note that an appreciable σ_{IS} appears to be able to induce settling at the slag/steel interface, a situation necessary for inclusion re-entrainment back into the steel. One of the assumptions in these two figures is that dissolution of the inclusion only begins after particle settling, and particle position is constant during dissolution.

As can be seen, this assumption of constant size during settling may not be valid, as the inclusion radius has decreased a small but non-negligible amount before complete particle settling. This conclusion has encouraged the combination of dissolution and separation, in which the current interfacial area between inclusion and slag allows the calculation of the proper amount of dissolution at each step. Subsequently, the model uses the new inclusion radius to calculate the motion variables for the next step, including dissolution. Figure 17 details separation and dissolution curves for the coupled model for the higher σ_{IS}. It should be noted that while separation appears to be decreasing, it is remaining at a constant *percentage* separation as it dissolves, and its top edge (from which Z is calculated) gets closer to the interface.

Also under examination is the effect of the formation of the steel film. Figure 18 shows separation and dissolution curves for a 20 μm-diameter spherical inclusion, using its terminal velocity of 1×10^{-4} m/s as its initial speed. In this case, a steel film does not form, and both ladle and mold slags allow the inclusion to separate while the tundish slag is viscous enough to slow and trap the inclusion. In Figure 19, the initial speed is chosen to be a higher value of 0.1 m/s, which causes a steel film to form ahead of the inclusion. The time at which the film ruptures is noted on the figure. Here, the same behavior between slags occurs, and separation times appear to be extremely similar. From comparison of these two charts, it seems apparent – unless increasing the initial speed perfectly negates the requirement of forming a steel film – that forming a steel film does not greatly affect the behavior of inclusions, at least in this case.

In all cases, it is apparent that a viscous slag will lengthen the separation time, as the tundish slag curves are pushed to longer times for all cases.

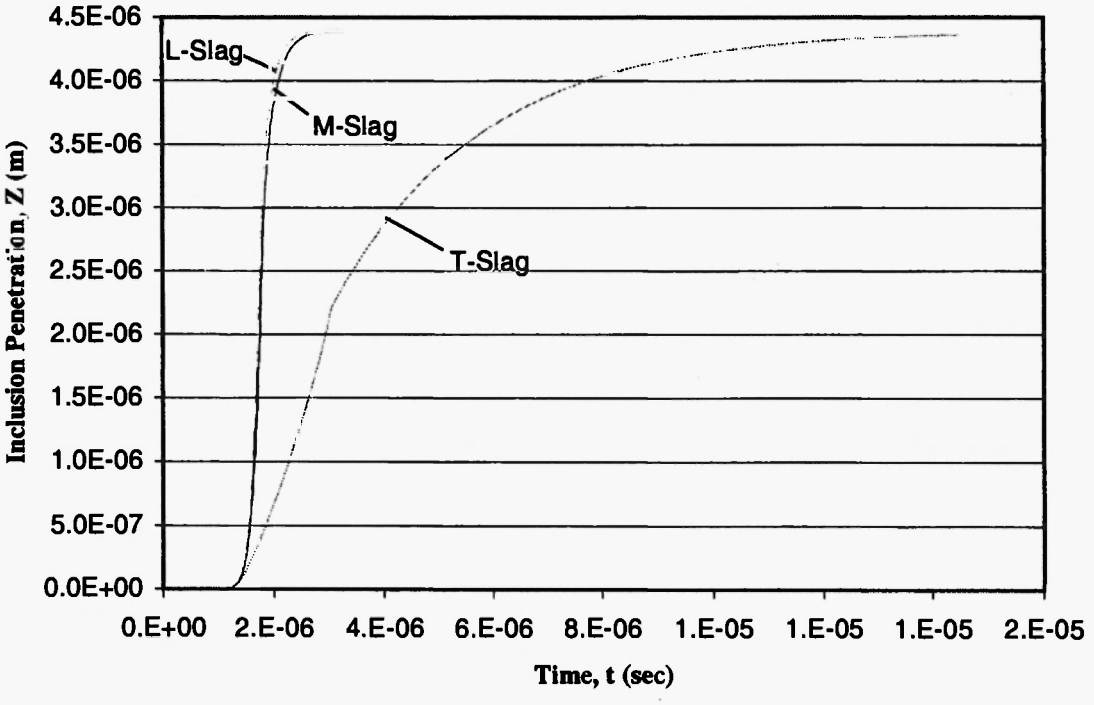

Fig. 11: Separation curve for an octahedron, with minimal (0.01 N/m) slag/inclusion interfacial energy.

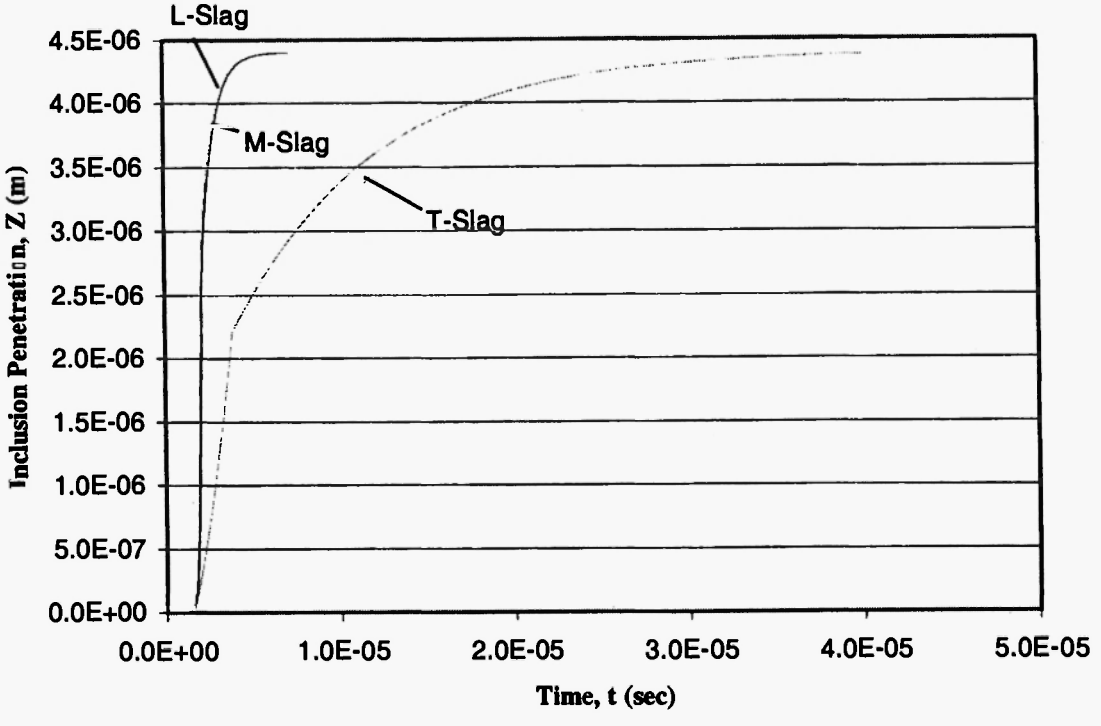

Fig. 12: Separation curve for an octahedron, with appreciable (0.6 N/m) slag/inclusion interfacial energy.

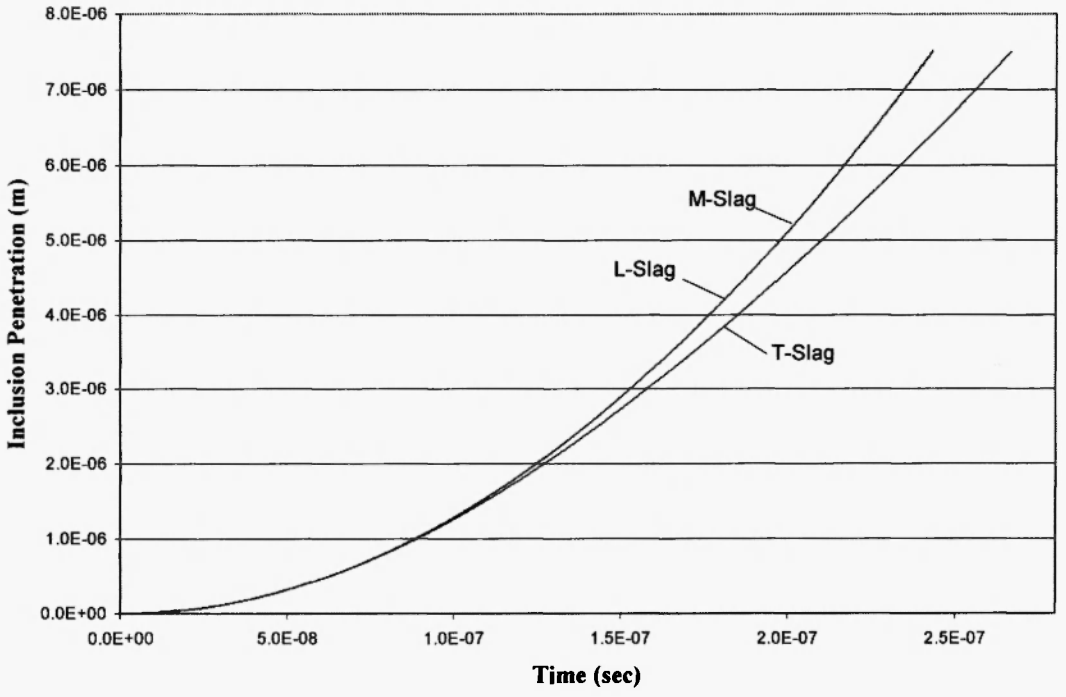

Fig. 13: Separation curve for a vertical plate, with appreciable (0.01 N/m) slag/inclusion interfacial energy

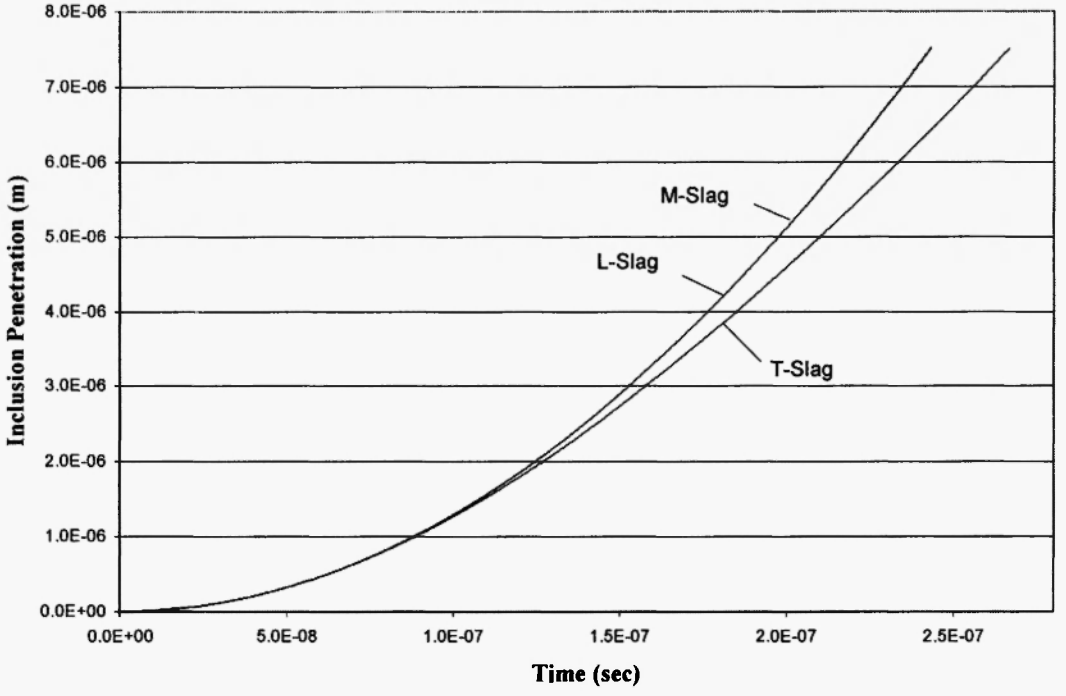

Fig. 14: Separation curve for a vertical plate, with appreciable (0.6 N/m) slag/inclusion interfacial energy

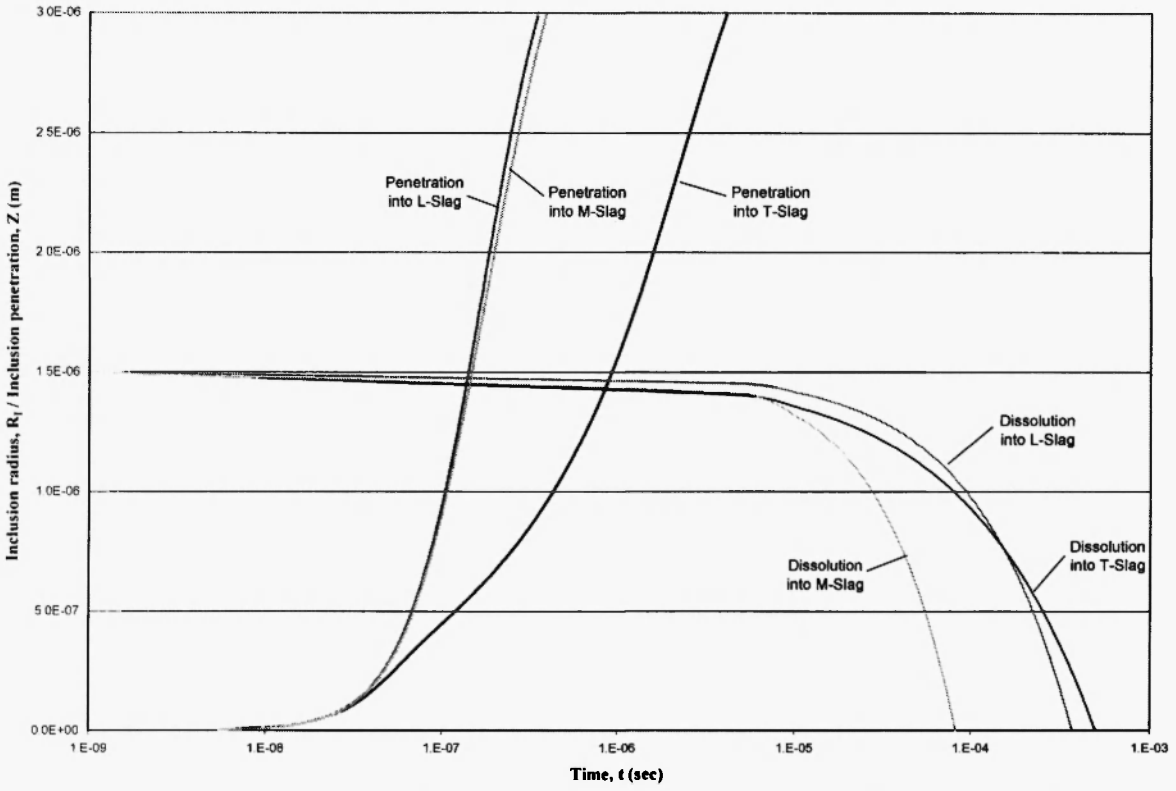

Fig. 15: Non-coupled separation and dissolution curve for a sphere of 1.5 micron radius, with minimal (0.01 N/m) slag/inclusion interfacial energy.

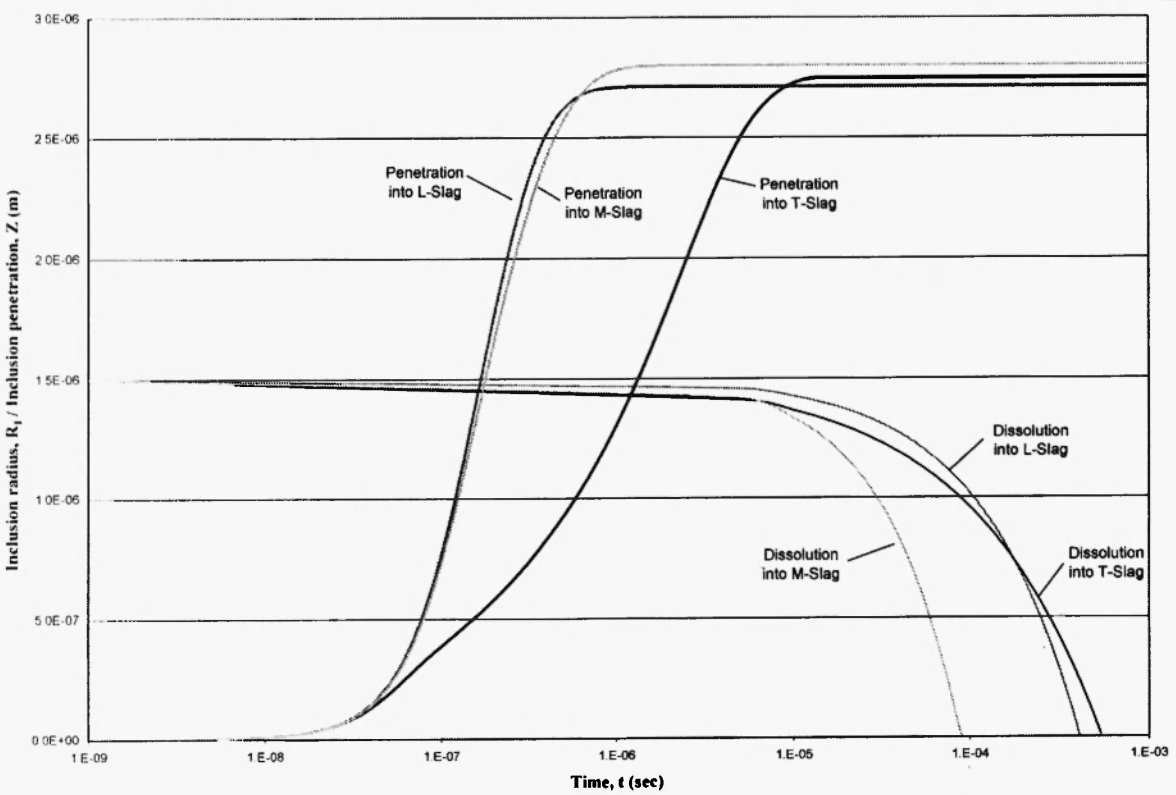

Fig. 16: Non-coupled separation and dissolution curve for a sphere of 1.5 micron radius, with appreciable (0.6 N/m) slag/inclusion interfacial energy.

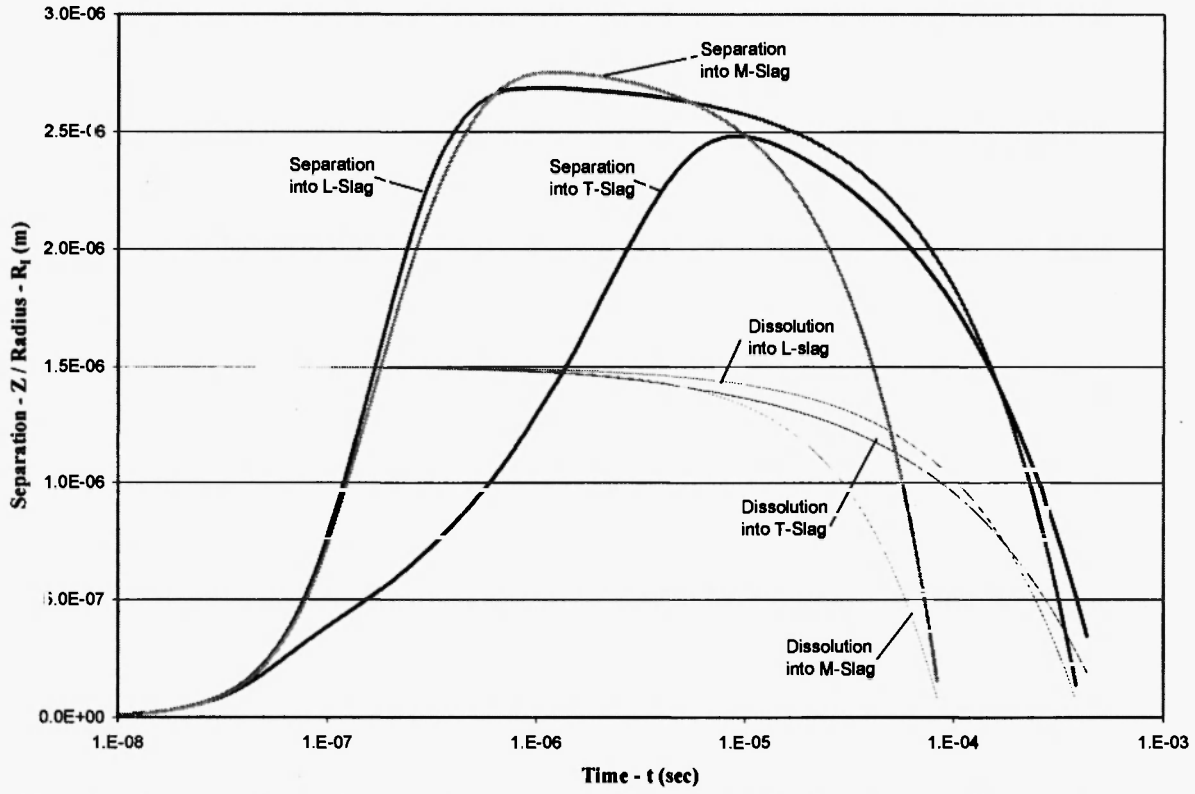

Fig. 17: Coupled separation and dissolution curve for a spherical inclusion with a radius of 1.5 microns, with appreciable (0.6 N/m) slag/inclusion interfacial energy.

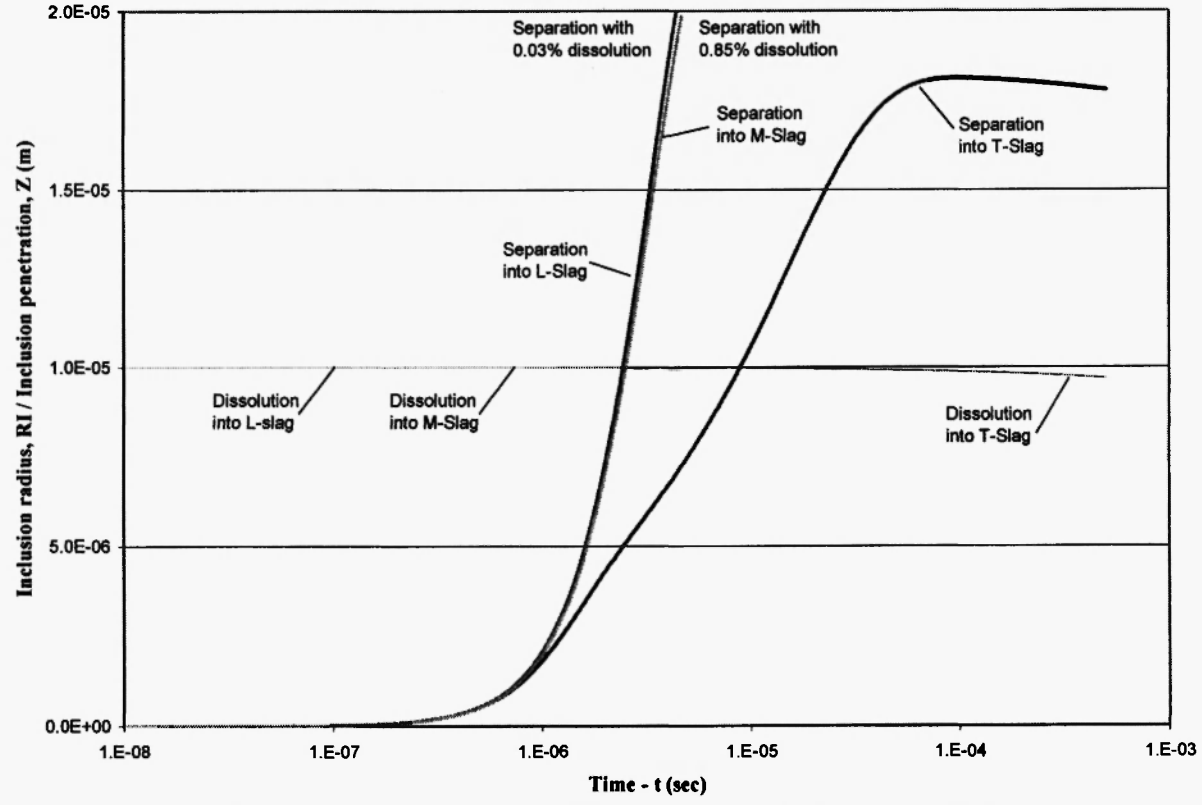

Fig. 18: Coupled separation and dissolution curve for a sphere with a radius of 10 microns that is initially at terminal velocity (1.E–4 m/s)and with appreciable (0.6 N/m) slag/inclusion interfacial energy.

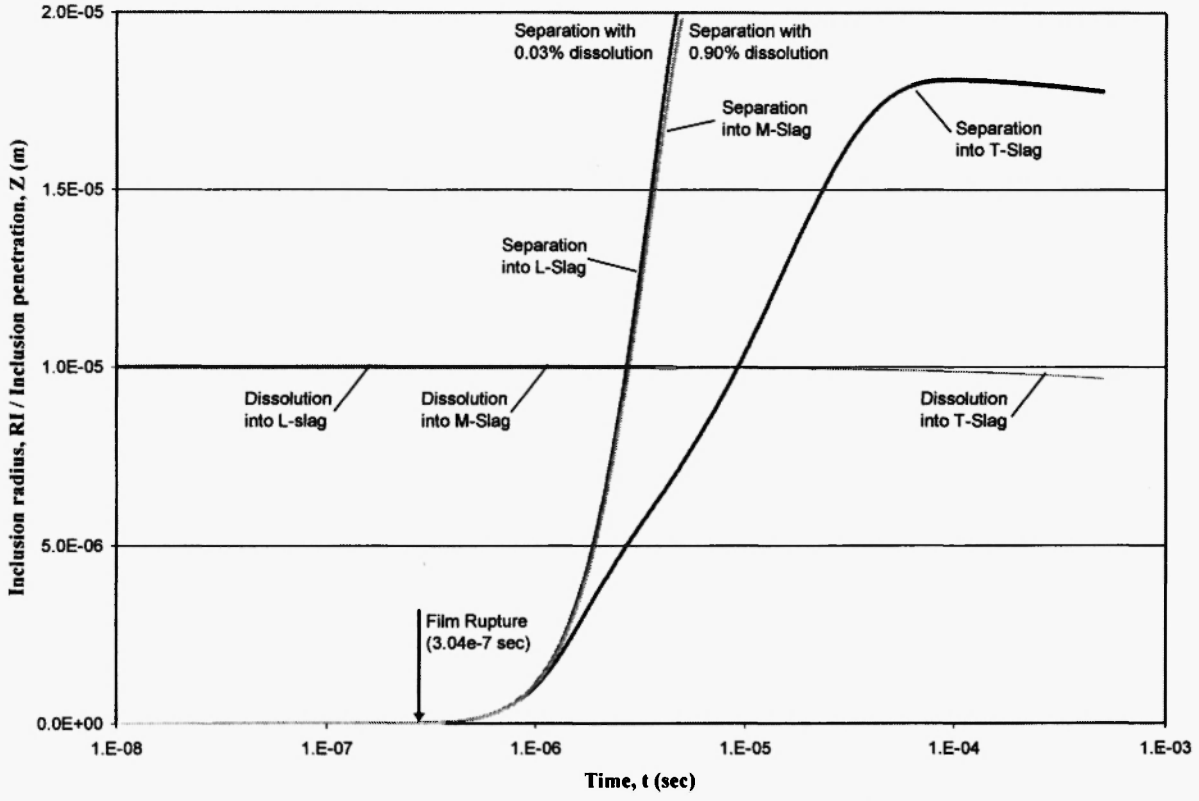

Fig.19: Coupled separation and dissolution curve for a sphere with a radius of 10 microns at 0.1 m/s initial velocity (thus forming a steel film) and with appreciable (0.6 N/m) slag/inclusion interfacial energy.

SUMMARY

In this examination of previously introduced inclusion separation models, we have (i) expanded a relatively simple model to include basic functionality for different inclusion shapes, (ii) examined the interfacial capillary force that has been shown to be an important (if not the most important) effect on inclusion separation behavior, (iii) included dissolution behavior of settled, spherical inclusions and shown non-coupled and coupled separation models, and (iv) compared film formation cases to non-film formation cases.

ACKNOWLEDGEMENTS

Financial support from the National Science Foundation under the CAREER grant DMR 0348818 is greatly acknowledged.

LIST OF SYMBOLS

Physical Properties

σ	Interfacial energy (N m)
ρ	Density (kg/m^3)
μ	Viscosity (kg/m s)
g	Acceleration due to gravity (m/s^2)
U_{term}	Terminal velocity of inclusion (m/s)
C_d	Drag coefficient
C_m	Fluid-mass damping coefficient
Re	Reynolds number
τ	Total dissolution time (s)
b	Dissolution mechanism exponent

Energies/Forces

G	Gibbs Free Energy (N m)
$E_{\sigma,Z}$	Interfacial Energy (N m)
$F_{\sigma,Z}$	Capillary Force (N)

F_d	Drag Force (N)
F_b	Buoyancy Force (N)
F_m	Fluid-mass damping force (N)

Geometric Symbols

R_I	Radius of sphere (m)
a	Edge length of octahedron (m)
s	Side length of plate (m)
Z	Inclusion penetration into slag (m)
A	Surface area (m^2)
V	Volume (m^3)

Subscripts

I	Inclusion
M	Metal
S	Slag

REFERENCES

1. P. Kozakevitch and L. Lucas, *Revue de Metallurgie*, 65, 589-598 (1968).
2. P. Kozakevitch and M. Olette, *Revue de Metallurgie*, 68, 636-646 (1971).
3. P. Kozakevitch and M. Olette, "Role of surface phenomena in the mechanism of removal of solid inclusions", *Production and Application of Clean Steel, Intl. Conference*, Balatonfured, Hungary, The Iron and Steel Institute, London, pp. 42-49, 1970.
4. P.V. Riboud and M. Olette, "Mechanisms of some of the reactions involved in secondary refining", *Proc. 7th International Conference on Vacuum Metallurgy*, Tokyo, Japan, pp. 879-889, 1982.
5. A.W. Cramb and J. Jimbo, "Interfacial considerations in continuous casting", *W.O. Philbrook Memorial Symposium*, Toronto, Ontario Canada, 17th – 20th April, ISS, Inc., Warrendale, pp. 259 – 271, PA, USA, 1988.
6. V.F. Chevrier, Overview of doctoral thesis, Department of Materials Science and Engineering, Carnegie Mellon University (1999)
7. S. Hartland, "Thin liquid films, fundamentals and applications", in: *Surface Science Series*, Vol. 29. Edited by: I.B. Iuvanov, Marcel Dekker Inc., NY, 1988.
8. Bouris, D., and Bergeles, G., "Investigation of Inclusion Re-Entrainment from the Steel-Slag Interface." *Metallurgical and Materials Transactions B*, vol.29B, June, pp. 641-649 (1998)
9. Nakajima, K. and Okamura, K., "Inclusion transfer behavior across molten steel-slag interface", 4th Intl. Conf. on Molten Slags and Fluxes, ISIJ, Sendai, pp. 505-510 (1992)
10. R. Dekkers, "Non-Metallic Inclusions in Liquid Steel", Doctoral Thesis, Katholieke Universiteit Leuven, Faculteit Wetenschappen, Dapartment Geografie-Geologie, Chapters 4 and 8, June, 2002.
11. A.B. Fox, M.E. Valdez, J. Gisby, R.C. Atwood, P.D. Lee and S. Sridhar, "Dissolution of ZrO_2, Al_2O_3, MgO and $MgAl_2O_4$ particles in a B_2O_3 containing commercial fluoride-free mould slag", *ISIJ International*, in press (2003).
12. M. Valdez, K. Propakorn, A.W. Cramb and S. Sridhar, "Study of the dissolution of alumina particles in CaO-Al_2O_3-SiO_2-MgO slags", *Ironmaking and Steelmaking*, 29 (2), 47-53 (2002).
13. K.C. Mills *et al.* "*Slag Atlas*", 2nd Edition, Veren Deutscher Eisenhüttenleute (VDEh), Verlag Stahleisen , Düsseldorf, GmbH, 1995.
14. Guthrie, R.I.L. "*Engineering in Process Metallurgy*", Oxford Science Publications, Clarendon Press, Oxford, UK, 1989.